ADVANCED FUNCTIONAL MATERIALS
www.afm-journal.de

Substrate Curvature-Induced Regulation of Charge Distribution of Covalent Organic Frameworks Promotes Capacitive Deionization

Dong Jiang, Ruibo Xu, Liang Bai, Jonathan P. Hill, Joel Henzie, Liyang Zhu, Wei Xia, Ran Bu, Yingji Zhao, Yunqing Kang, Takashi Hamada, Renzhi Ma, Nagy Torad, Jie Wang, Toru Asahi, Xingtao Xu,* and Yusuke Yamauchi**

Covalent organic frameworks (COFs) are promising high-performance capacitive deionization (CDI) materials. Strategies to optimize CDI performance of COFs focus largely on hybridization with conductive substrates, to improve their their intrinsically poor conductivity. A new structure-function relationship between COFs and their substrates is proposed here based on substrate-induced surface curvature. Graphene (zero-curvature) and carbon nanotubes (CNT, curved) are selected as COF growthsubstrates to assess the effect of curvature engineering effect on CDI performance of TpPa-SO_3H-COF. Ultrahigh ion (Na^+) adsorption capacity (58.74 mg g^{-1}) is achieved by CNT-COF hybrid (*cf.* compared to graphene-COF hybrid 34.20 mg g^{-1}), demonstrating the significance of curvature engineering. Notably, the corresponding salt (NaCl) adsorption capacity of CNT-COF hybrid reaches 149.25 mg g^{-1} in 1000 ppm at 1.2 V, representing state-of-the-art CDI performance, and the highest value among organic CDI electrodes. X-ray photoelectron spectroscopy and theoretical calculations subsequently reveal that substrate curvature can induce local strain, which regulates charge distribution within the COF skeleton, causing a lower binding energy state for Na^+ adsorption. Electrochemical quartz crystal microbalance measurements revealed faster Na^+ adsorption kinetics of CNT-COF due to regulated charge distribution within COF skeleton induced by substrate curvature. This work gives new insight into design of COF materials based on curvature engineering.

1. Introduction

The growing demand for fresh water in agriculture, industry, and other sectors necessitates the rapid development of technologies that can be used to produce clean water from challenging sources including seawater, wastewater, or brackish water.[1–5] Capacitive deionization (CDI) has emerged as a promising environmentally friendly, low-energy process to address the global shortage of freshwater.[6,7] In contrast to other energy-intensive technologies such as reverse osmosis (RO), CDI removes ions from saline water using a capacitor consisting of pairs of oppositely-charged electrodes where electrosorption[8] or redox reactions occur.[9,10] CDI is gaining traction as an alternative to established desalination technologies. It is particularly effective for applications at salt concentrations below 10 g L^{-1}, such as in households or small businesses where trained operators are unavailable. CDI operates at low pressures and temperatures, using voltages that are compatible with standard consumer electrical

---

D. Jiang, L. Zhu, Y. Zhao, Y. Kang, T. Hamada, Y. Yamauchi
Department of Materials Process Engineering
Graduate School of Engineering
Nagoya University
Furo-cho, Chikusa-ku, Nagoya, Aichi 464-8603, Japan
E-mail: y.yamauchi@uq.edu.au

D. Jiang, L. Zhu, Y. Zhao, T. Asahi
Faculty of Science and Engineering
Waseda University
3-4-1 Okubo, Shinjuku, Tokyo 169-8555, Japan

The ORCID identification number(s) for the author(s) of this article can be found under https://doi.org/10.1002/adfm.202407479

DOI: 10.1002/adfm.202407479

R. Xu, L. Bai, X. Xu
Marine Science and Technology College
Zhejiang Ocean University
Zhoushan 316022, P. R. China
E-mail: xingtao.xu@zjou.edu.cn

J. P. Hill, J. Henzie, R. Ma, N. Torad
Research Center for Materials Nanoarchitechtonics
National Institute for Materials Science
Namiki, Tsukuba, Ibaraki 305-0044, Japan
E-mail: jonathan.hill@nims.go.jp

W. Xia
School of Chemistry and Chemical Engineering
Anhui University of Technology
Ma'anshan 243032, P. R. China

equipment, enhancing its applicability and ease of use.[9] The development of new electrode materials, which are the critical components of CDI systems promoting adsorption performance, is a highly active research area. Carbon-based materials, including activated carbon, carbide-derived carbons, carbon nanotubes (CNTs), and graphene have all been successfully applied for the fabrication of CDI electrodes.[11–14] However, conventional porous carbon-based electrodes often suffer from ion adsorption capacity bottleneck issues resulting from a limitation of salt adsorption capacity (SAC) based on electric double layers (EDLs).[15–17] To overcome this limitation, the introduction of new electrode materials having higher SACs, but which are also capable of immobilizing ions by several mechanisms rather than solely through electrosorption, is highly desirable.

Electrode materials based on covalent organic frameworks (COFs), a versatile class of crystalline porous 2D or 3D polymeric organic frameworks, are promising candidates for the next generation of sustainable CDI systems with enhanced SACs based on their molecular design flexibility, which permits tuning of their physical and chemical properties.[18–20] In contrast to traditional polymers which lack ordered porosity, COFs possess high porosity, uniform pore sizes, and high structural modularity, which are advantageous in establishing appropriate electrochemical performances and improved diffusion of molecules/ions to active sites.[21–24] For these reasons, COFs are widely studied in the fields of batteries, supercapacitors, and other energy storage applications. More recently, some pioneering works have demonstrated the use of COFs for CDI electrodes, achieving SACs of 29.34 mg g^{-1} for covalent triazine-based frameworks[25] and 22.8 mg g^{-1} for 2,6-diaminoanthraquinone-1,3,5-triformylphloroglucinol (Tp)-COF.[26] At this stage, the SACs of COFs can only be comparable to carbons, which is far below the expected value.

Generally, most COFs have limited intrinsic conductivities even if bulk aggregation induced by π–π stacking is overcome by exfoliating COFs; this is recognized as the main reason causing poor CDI performance. Hybridization of COFs with conductive substrates/additives has addressed this issue due to improved electron and mass transfer characteristics.[27] Many of these works are aimed at the composite engineering of COFs and carbon, and revealed that the carbon substrate has a strong influence on the physical and chemical properties of the COFs.[28–31] For example, a composite of a polyimide COF and CNT showed a 71% utilization of redox-active sites for Li-ion batteries, a great improvement over the pure polyimide COF where a 5% utilization of active sites was found under the same conditions.[29] In addition to the high electrical conductivity of CNT, another important parameter leading to this enhancement may be the surface curvature of CNT. As a widely studied approach in inorganic electrocatalysts, surface curvature engineering of active sites has demonstrated a novel structure-function relationship that enables better electrochemical reactions. Unfortunately, however, the related correlation between the structural characteristics of carbon templates and the resulting properties of the COF composites has received limited attention thus far. A detailed structure-function relationship affecting the various properties still remains obscure.

In this work, we demonstrate that substrate curvature has a significant role in affecting the properties of COF (**Figure 1**). Graphene and CNT, possessing well-defined and uniform sp^2-hybridized carbon frameworks,[32] are selected as model substrates here for the exploration of structure-function relationships of COF-based materials. In contrast to graphene, the unique feature of the curved CNT substrate imparts curvature to the in situ grown COF skeleton, which in turn affects the chemical properties of the resulting composite.[33–35] As a result, the CNT-COF material exhibited a remarkable CDI performance including an ion (Na^+) adsorption capacity (IAC (Na^+)) of 58.74 mg g^{-1} and ion (Na^+) adsorption rate (IAR (Na^+)) of 1.96 mg g^{-1} min^{-1} in 1000 ppm NaCl solution at 1.2 V, accompanied by a substantial SAC of 149.25 mg g^{-1} for the whole cell. From a theoretical insight, such a performance improvement is ascribed to the fact that substrate curvature could induce local strain and regulation of charge distribution within the COF skeleton causing a lower binding energy state for Na^+ adsorption. Notably, this ultrahigh Na^+ adsorption capacity is significantly better than those of almost all the reported organic-based materials (For a comparison see Table S1, Supporting Information). This work demonstrates the significance of substrate curvature for the design of superior CDI electrodes and also inspires further consideration of the structure-function relationship of COF-based materials.

2. Results and Discussion

2.1. Materials Design and Characterization

TpPa-SO_3H-COF was synthesized by the Schiff-base condensation reaction of Tp with 1,4-phenylenediamine-2-sulfonic acid (Pa-SO_3H) to give a crystalline 2D COF in 91% yield (Figure S1 and see the experimental details in the Supporting Information).[36] The condensation reaction was followed by an irreversible keto-enol tautomerization, which enhances the chemical stability and reduces the solubility of the COF.[37–39] Solvent plays a critical role in the crystallinity of the COF and the morphology of the corresponding CNT-COF core-shell structure. After optimization, a mixed solvent system (1,4-dioxane/mesitylene = 1:4 (v/v)) containing 6 M acetic acid as a catalyst at 120 °C was found to yield the COF with suitable crystallinity or the CNT-COF composites having a well-formed core-shell structure. Different quantities of CNT were added to produce TpPa-SO_3H@CNT-X, where X = 10, 30, 50, and 70 wt.% of CNT. For this study, catalyst-free, multi-walled CNT were used with 50–60 nm outer diameter and a length range of 0.5–10 μm. In the presence of a carbon substrate, the COF tends to grow on the surfaces of the CNT or graphene substrates induced by π–π

R. Bu
State Key Laboratory of Chemical Engineering
Institute of Pharmaceutical Engineering
College of Chemical and Biological Engineering
Zhejiang University
Hangzhou 310027, P. R. China

J. Wang, Y. Yamauchi
Australian Institute for Bioengineering and Nanotechnology (AIBN)
The University of Queensland
Brisbane, QLD 4072, Australia

Y. Yamauchi
Department of Chemical and Biomolecular Engineering
Yonsei University
Yonsei-ro, Seodaemungu, Seoul 03722, South Korea

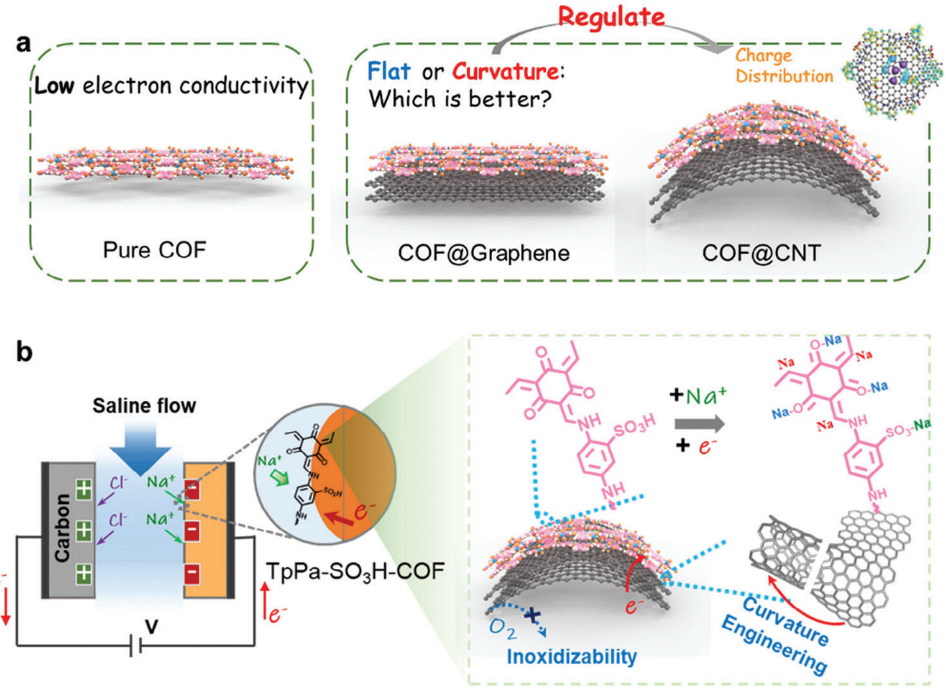

Figure 1. Regulation of charge distribution of COF promotes CDI performance. a) Substrate curvature-induced engineering for the regulation of charge distribution of COF, b) CDI process at the curvature COF-based electrode which presents the advantages of oxidation resistance, high electron conductivity, and Na^+ ion adsorption.

interactions between the COF and the carbon substrates. Local interactions between the curved CNT and the contacting COF layer result in some distortion of the COF structure. Details of the structure and morphologies of the different materials are shown in **Figure** 2a–h.

The simulated structure of porous crystalline TpPa-SO_3H-COF is shown in Figure 2a. In the structure, its hexagonal pores are stacked along the c-axis with some slight slippage from an eclipsed configuration. Fourier-transform infrared spectroscopy (FTIR) was used to confirm the successful condensation of TpPa-SO_3H-COF and TpPa-SO_3H@Carbon composites. As shown in Figure 2b, the absence of N-H stretching bands at 3429, 3403 and 3337 cm^{-1} from the Pa-SO_3H precursor in TpPa-SO_3H-COF and any TpPa-SO_3H@Carbon composites indicates the complete consumption of Pa-SO_3H in the polycondensation reactions. The strong formyl C═O vibration band observed for Tp (≈1650 cm^{-1}) is almost absent in the TpPa-SO_3H-COF, while the weak but observable peak could be due to residual C═O bonds at the edges of the structure. The peaks at 1282 and 1579 cm^{-1} in the spectrum are due respectively to β-ketoenamine C—N moieties and C═C groups, suggesting that the COF exists in a β-ketoenamine form.[40,41] This result was further confirmed by the resonance (CP-MAS ^{13}C NMR) measurements, showing the characteristic peak at 184 ppm ascribed to the carbon atom of keto (—C═O) group (Figure S2, Supporting Information) Furthermore, X-ray photoelectron spectroscopy (XPS) was conducted to study the binding energy of different elements in TpPa-SO_3H-COF, especially for oxygen which is present at the main sodium adsorption site in the framework. As shown in Figure S3 (Supporting Information), the O 1*s* spectra for TpPa-SO_3H-COF can be deconvoluted to two peaks centered at 530.24 and 531.87 eV, corresponding respectively to C═O and S—O groups, respectively. Significantly, compared to TpPa-SO_3H@Graphene, both peaks in TpPa-SO_3H@CNT-50 show a shift to lower binding energy. This evidence indicates that the adsorption sites in the curved COF induced by CNT could be more active for Na^+ adsorption than those in TpPa-SO_3H@Graphene. This will be discussed in more detail below.

Powder X-ray diffraction (PXRD) was used to confirm the structure of the TpPa-SO_3H-COF and its crystallinity in the TpPa-SO_3H@Carbon composites. The experimental PXRD pattern of TpPa-SO_3H-COF closely matches the simulated PXRD pattern of the aligned A-A stacking model (Figure 2c). The characteristic diffraction peaks at $2\theta = 4.6°$ and 26.2° are assigned to the (100) and (001) planes which represent the pore structure and layer stacking, respectively. The peak broadening and difference in the peak intensity ratio between the experimental and simulated patterns may be due to the small particle size of the TpPa-SO_3H powders and some deviation from a perfect crystalline structure and is consistent with previous reports.[42] The PXRD patterns of the TpPa-SO_3H@Carbon composites show that the addition of the carbon substrate lowers the crystallinity of TpPa-SO_3H-COF, with TpPa-SO_3H@CNT-70 being the least crystalline according to PXRD data (Figure S4a, Supporting Information). The strong peaks ≈26.1° and 26.4° for TpPa-SO_3H@CNT-50 and TpPa-SO_3H@Graphene represent the (002) plane for CNT and Graphene respectively (Figure S4b, Supporting Information). However, the PXRD patterns indicate that TpPa-SO_3H-COF maintains the same structure in the COF@Carbon composites. The morphologies of TpPa-SO_3H-COF, TpPa-SO_3H@CNT-X, and TpPa-SO_3H@Graphene were observed by using a scanning electron microscope (SEM, Figure 2d–i; Figure S5,

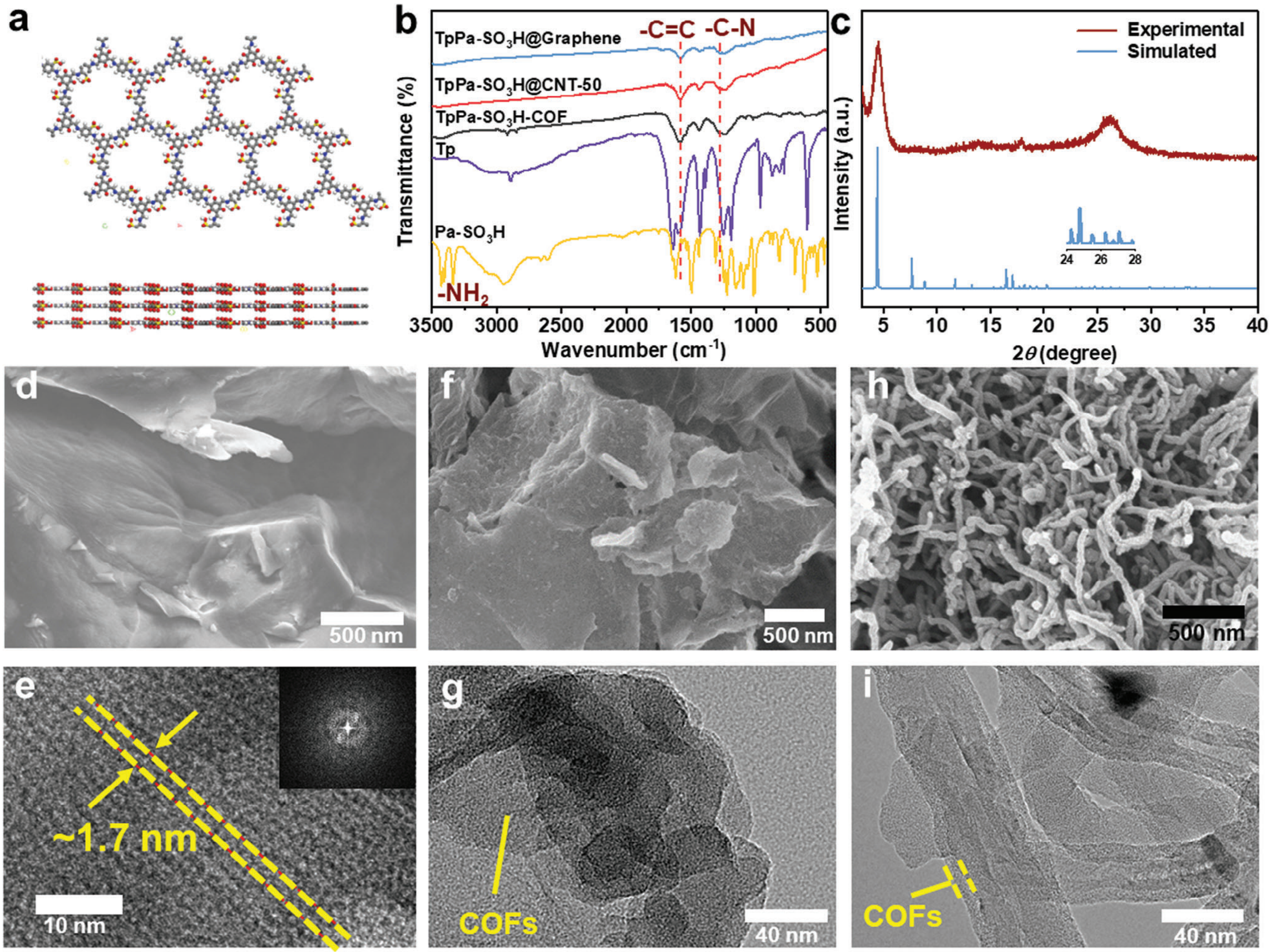

Figure 2. Structural evolution characterization of TpPa-SO_3H-COF, TpPa-SO_3H@CNT-50 and TpPa-SO_3H@Graphene a) the simulated structure of TpPa-SO_3H-COF. b) FTIR characterization of the building blocks for constructing COFs and the as-prepared TpPa-SO_3H-COF, TpPa-SO_3H@CNT-50, and TpPa-SO_3H@Graphene.c) XRD patterns of the as-prepared TpPa-SO_3H-COF. Red cycles: experimental PXRD pattern, blue line: computational simulation. d) SEM image of TpPaSO_3H-COF. (e) HR-TEM image and corresponding FFT pattern of TpPa-SO_3H-COF. f,g) SEM and TEM images of TpPa-SO_3H@Graphene. h,i) SEM and TEM images of TpPa-SO_3H@CNT.

Supporting Information). TpPa-SO_3H-COF has a bulk solid rather featureless morphology while, in contrast, the TpPa-SO_3H-COF appears to grow on the surfaces of the carbon substrates when CNT and graphene are present during synthesis leading to corresponding plate-like and fibre-like morphologies. Tube-type core-shell structures of TpPa-SO_3H@CNT-X having the COF structure grown around the external surface of the CNT could be observed (Figure 2h–I; Figure S6, Supporting Information).

N_2 adsorption-desorption isotherms were measured to investigate the porosities of TpPa-SO_3H-COF, TpPa-SO_3H@CNT-50, and TpPa-SO_3H@Graphene (Figure S7, Supporting Information). Compared to the pristine TpPa-SO_3H (specific surface area = 220.62 m^2 g^{-1}), the specific surface area of TpPa-SO_3H@CNT-50 decreases slightly to 195.66 m^2 g^{-1}. but increases to 317.67 m^2 g^{-1} in TpPa-SO_3H@Graphene. This difference might be caused by the different properties of the CNT and graphene substrates. The addition of CNT has a slight effect on the specific surface area with values of 176.03, 196.13, 195.66, and 218.21 m^2 g^{-1} found, respectively, for TpPa-SO_3H@CNT-10, TpPa-SO_3H@CNT-30, TpPa-SO_3H@CNT-50 and TpPa-SO_3-H@CNT-70.

2.2. Sodium Storage Mechanism in the Framework

It is necessary to understand the sodium storage mechanism of the COF before studying their electrochemical properties and CDI performances. Hence, ex situ FTIR was performed to investigate any structural evolution during charge/discharge processes involving sodium ions. The scheme shown in **Figure 3a** indicates that the Na^+ insertion mechanism in pure TpPa-SO_3H-COF involves the transportation of six electrons and one proton, thus offering seven Na^+ charge/discharge active sites. As shown in Figure 3b, there are three different active sites for Na^+ adsorption in the COF structure. A new peak ≈1710 cm^{-1} after sodium adsorption suggests the formation of -SO_3Na, which is a result of the cation exchange reaction during the capture processes.[43] The carbonyl O atoms of the β-keto units receive electrons and

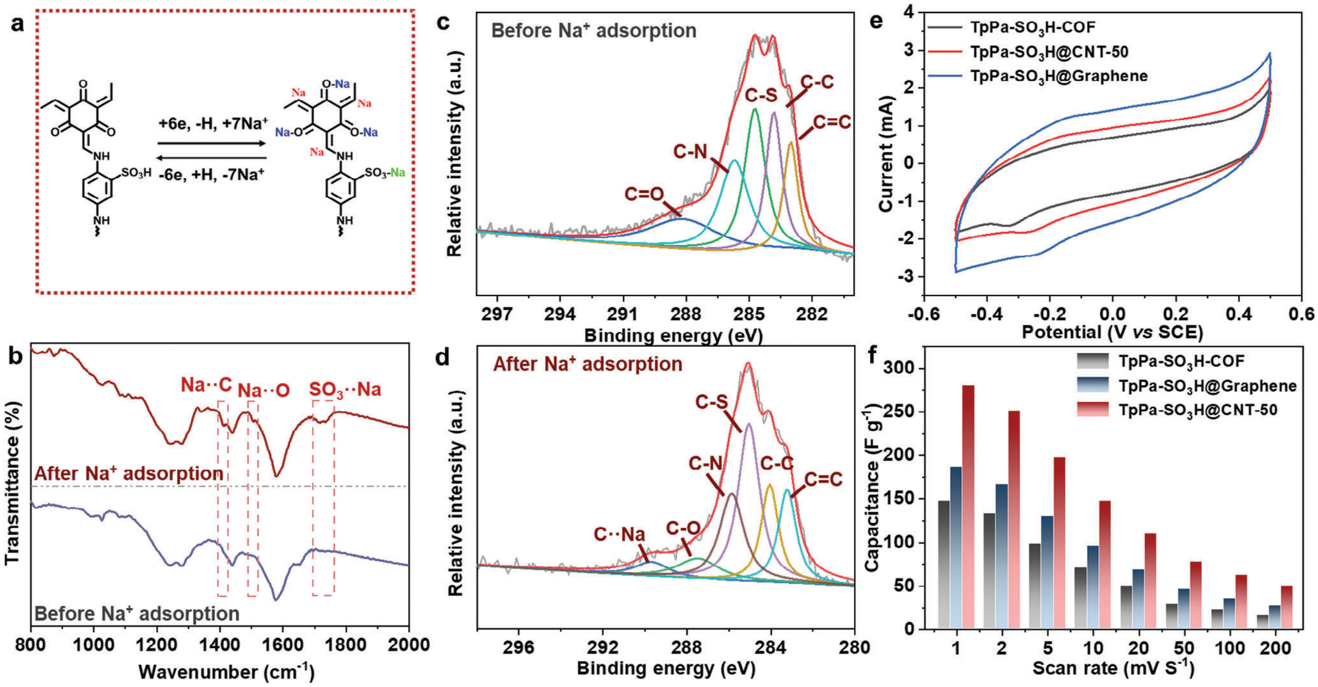

Figure 3. Confirmation of the sodium adsorption sites in the TpPa-SO_3H-COF structure. a) Na^+ insertion mechanism of pure TpPa-SO_3H-COF. b) FTIR characterization of TpPa-SO_3H-COF before and after sodium ions adsorption. c,d) XPS spectra of the C 1s region of TpPa-SO_3H-COF before and after sodium ions adsorption. e) CV curves of TpPa-SO_3H-COF, TpPa-SO_3H@CNT-50, and TpPa-SO_3H@Graphene. f) Capacity based on CV curves of CV curves of TpPa-SO_3H-COF, TpPa-SO_3H@CNT-50, and TpPa-SO_3H@Graphene.

can coordinate sodium ions, as indicated by the new peak ≈1500 cm^{-1} after Na^+ adsorption, and which also further form α-C radicals stabilized by the enamine units and aromatic rings. The electrophilic α-C radicals subsequently accept additional electrons to form α-C anions, which can bind further sodium ions (1410 cm^{-1}).

To investigate in more detail, X-ray photoelectron spectroscopy (XPS) spectra of TpPa-SO_3H-COF were collected prior to and following Na^+ adsorption. As shown in Figure 3c,d, the C 1s spectra are deconvoluted into five peaks at 288.14, 284.73, 283.83, 283.03, and 283.71 eV for the as-prepared TpPa-SO_3H-COF electrodes, assigned to C═O, C—S, C—C, C═C, and C—N bonding modes, respectively. After sodium insertion, the carbon-oxygen bond shifts to 287.42 eV, implying a reduction of C═O to C—O, which is consistent with results obtained from FTIR spectra.[44] Also, an additional peak emerges at 289.63 eV, assigned to α-C – Na interaction, which results from the insertion of sodium ions at the C atoms of β-ketoenamine groups.[45] These observations are consistent with previously reported observations occurring during sodium ion charge/discharge at organic electrodes.[46,47]

2.3. Electrochemical Characterization

The electrochemical properties of TpPa-SO_3H-COF and the related carbon hybrids were first investigated by cyclic voltammetry (CV) in the −0.5 –0.5 V range. The three-electrode system used comprises an aqueous 1 M NaCl solution as the electrolyte, a Pt electrode as the counter electrode, and a saturated calomel electrode as the reference electrode. The CV curves in Figure 3e contain a pair of quasi-reversible redox peaks for the TpPa-SO_3H-COF and TpPa-SO_3H@Carbon hybrid structures. These peaks correspond to redox processes of the COF structure involving the Na^+ ions of the NaCl electrolyte as mentioned above. The adsorption sites in the COF structure confer excellent reversible charge/discharge of sodium ions on the COF and TpPa-SO_3H@Carbon hybrid structures, making them suitable for potential CDI applications. Additionally, the redox peak of TpPa-SO_3H@CNT-50 shifts to zero potential compared with that of TpPa-SO_3H@Graphene and pristine TpPa-SO_3H COF, indicating easier activation of the adsorption sites in TpPa-SO_3H@CNT-50. Furthermore, the integrated area of the CV curve of the TpPa-SO_3H@CNT-50 hybrid is larger than those of pristine COF and TpPa-SO_3H@Graphene, which suggests that the CNT-induced curved TpPa-SO_3H COF will have improved capacitive performance and higher capacitance (Figure 3f). We further summarized the surface-controlled/diffusion-controlled processes in charge storage from the CV curves (Figure S8, Supporting Information). Obviously, as the scan rate increases, there is a corresponding increase in capacitive contributions for all of the samples. Notably, the capacitive contribution of TpPa-SO_3H@CNT-50 is higher than that of TpPa-SO_3H@Graphene and TpPa-SO_3H-COF, verifying that there is greater surface-controlled capacitive behavior generated by the substrate curvature-induced regulation of charge distribution of the framework. Galvanostatic tests of TpPa-SO_3H-COF, TpPa-SO_3H@CNT, and TpPa-SO_3H@Graphene at various rates were used to further study the charge/discharge process for these electrodes. The GCD curves are consistent with the CV curves as the TpPa-SO_3H@CNT-50 electrode achieves the longest discharge time indicating the

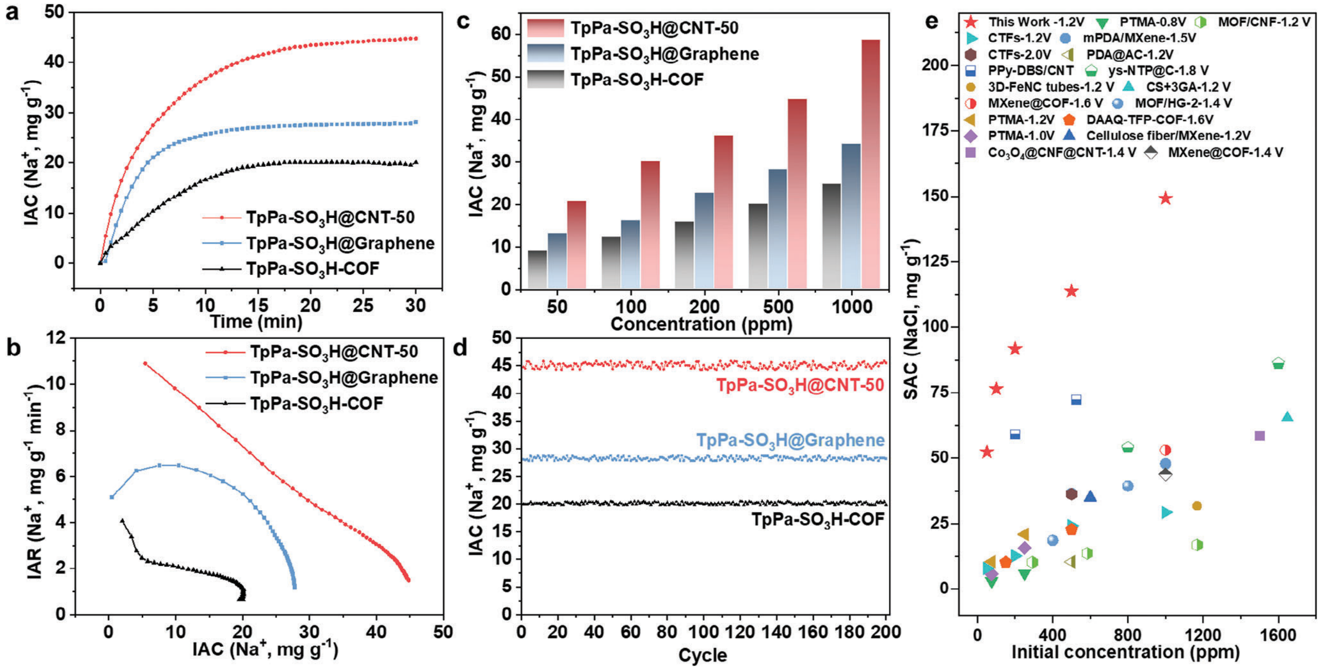

Figure 4. CDI performance of TpPa-SO_3H-COF, TpPa-SO_3H@CNT-50 and TpPa-SO_3H@Graphene. (a) Temporal variations in IAC (Na^+) of the materials, and (b) the corresponding Ragone plots for TpPa-SO_3H-COF, TpPa-SO_3H@CNT-50 and TpPa-SO_3H@Graphene in 500 ppm (8.55 mM) NaCl solution. (c) Sodium chloride concentration dependency of CDI performance. (d) Cycling performance in 500 ppm (8.55 mM) NaCl solutions. (e) Comparison of the desalination capacity of TpPa-SO_3H@CNT-50 with other organic materials or carbon-based electrodes (The listed samples are listed in Table S1, Supporting Information).

highest capacitance compared to the pure TpPa-SO_3H-COF and TpPa-SO_3H@Graphene electrodes (Figure S9, Supporting Information). Electrochemical impedance spectra (EIS) further reveal the merits of curvature engineering on the capacitive behavior. As shown in Figure S10 (Supporting Information), the fitted line for Z' versus square root of frequency ($\omega_{1/2}$) in the low-frequency region shows a steeper gradient for the curved TpPa-SO_3H-COF induced by CNT, indicating it has lower resistivity than both pure COF and then COF@Graphene hybrid.[48] This means that TpPa-SO_3H@CNT-50 has a larger ion diffusion rate again suggesting it is a promising candidate for capacitive deionization.

2.4. CDI Performance

As a proof-of-concept, asymmetric CDI devices containing either of the active materials TpPa-SO_3H@CNT-50 or TpPa-SO_3H@Graphene as the cathode for Na^+ capture, with AC as the anode for Cl^- capture, were constructed. For comparison, CDI cells using CNT or Graphene as one electrode were also operated under similar conditions., The asymmetric CDI configuration more easily achieved improved desalination performance than the symmetric CDI configuration due to a higher safe operating voltage and greater flexibility in the choice of electrode materials for higher Na^+ or Cl^- selectivity. These features also make it more suitable for the in-depth study of the cation charge/discharge process in the cathode. The desalination performance of all devices was conducted at an initial NaCl concentration of 500 ppm at 1.2 V, which is an acceptable operating voltage for asymmetric CDI cells. The corresponding conductivity and current profiles are shown in Figure S11 (Supporting Information). During the CDI process, no bubbles were observed, indicating that no side reactions such as chlorine generation or hydrogen evolution were occurring. The influence of the thickness of the COF on its CDI performance was investigated initially. As shown in Figure S12 (Supporting Information), TpPa-SO_3H@CNT-50 shows the highest Na^+ capacity with an IAC of 44.79 mg g^{-1} within 30 min. Further decreasing the thickness of COF by adding more CNT should not increase the overall capacity. However, it is worth noting that the materials with the thinnest COF components display higher adsorption rates within the first few minutes. This could be due to better electrochemical accessibility of active sites for the materials having thinner COF outer layers on the CNT.[37] After optimizing the effects of thickness on the CDI performance, the effects of curvature engineering on performance were investigated. **Figure 4** shows the desalination performances of TpPa-SO_3H-COF, TpPa-SO_3H@CNT-50 and TpPa-SO_3H@Graphene. TpPa-SO_3H@CNT-50 exhibits a high IAC (Na^+) of 44.79 mg g^{-1}, which is much greater than those found for TpPa-SO_3H@Graphene (28.12 mg g^{-1}) and pure TpPa-SO_3H-COF (20.04 mg g^{-1}) (Figure 4a). For the whole CDI cell, the TpPa-SO_3H@CNT-50 also shows a high SAC of 113.8 mg g^{-1}, far exceeding those of TpPa-SO_3H-COF (50.92 mg g^{-1}) and TpPa-SO_3H@Graphene (71.45 mg g^{-1}) (Figure S13, Supporting Information). As shown in Figure 4b, the corresponding CDI Ragone plots of TpPa-SO_3H@CNT-50 shift toward the upper right region suggesting higher IAC (Na^+) and faster IAR (Na^+) than those of pristine TpPa-SO_3H-COF and TpPa-SO_3H@Graphene, highlighting the enhancement of CDI performance in curvature engineered COF with a carbon substrate. In contrast, the carbon substrate displays limited CDI performance, with SAC value of 8.1 mg g^{-1} for Graphene and 6.2 mg g^{-1} for CNT (Figure S14, Supporting Information).

It is important to achieve excellent CDI performance over a wide range of concentrations because real-world feedwaters for practical CDI applications are usually brines of varying ionic strengths. Therefore, the CDI performance of TpPa-SO_3H-COF, TpPa-SO_3H@CNT-50, and TpPa-SO_3H@Graphene were further investigated using NaCl solutions having concentrations in the range from 50 to 1000 ppm, corresponding to a NaCl salinity window of 0.86 to 17.11 mM. As expected, all three samples exhibited increasing IAC values with increasing NaCl concentration. In particular, TpPa-SO_3H@CNT-50 exhibits an ultrahigh IAC (Na^+) of 58.74 mg g^{-1} and IAR (Na^+) of 1.96 mg g^{-1} min^{-1} in 1000 ppm NaCl solution, together with a very high SAC (NaCl) of 149.25 mg g^{-1} for the whole cell (Figure 4c; Figure S15, Supporting Information). This performance is significantly higher than those of TaPa-SO_3H-COF (IAC (Na^+): 24.8 mg g^{-1}; SAC (NaCl): 63.01 mg g^{-1}) and TpPa-SO_3H@Graphene (IAC (Na^+): 34.20 mg g^{-1}; SAC (NaCl): 86.87 mg g^{-1}). We further conducted the CDI test for TpPa-SO_3H-COF, TpPa-SO_3H@CNT-50, and TpPa-SO_3H@Graphene at various voltages. With an increase in the operating voltage, the sodium adsorption capacity of TpPa-SO_3H-COF, TpPa-SO_3H@CNT-50, and TpPa-SO_3H@Graphene all increase, with the TpPa-SO_3H@CNT-50 hybrid having consistently the highest capacity among these electrodes (Figure S16, Supporting Information). Long-term cycling stability is also an important criterion for estimating practical performance. Here, the long-term cycling property of the optimized hybrid, TpPa-SO_3H@CNT-50, was further evaluated at 1.2 V. For comparison, pure TpPa-SO_3H-COF and TpPa-SO_3H@Graphene were also studied under similar conditions. As shown in Figure 4d, all samples possess excellent cycling stability without obvious deterioration of performance even after 200 cycles. In addition, SEM images of the samples obtained after cycling (Figure S17, Supporting Information) indicate that all samples maintain their nanostructure even after long-term cycling. PXRD was used to further confirm that TpPa-SO_3H, TpPa-SO_3H@CNT-50, and TpPa-SO_3H@Graphene retained their crystallinity after the long-cycling operation. (Figure S18, Supporting Information) Notably, this ultrahigh Na^+ adsorption capacity is significantly better than those of almost all the reported organic-based materials (Figure 4e).

2.5. Discussion of Curvature Effects on CDI Performance

To gain a deeper insight into the origin of the enhancement of desalination properties of the curved TpPa-SO_3H@CNT-50, both experimental analysis and theoretical calculations were conducted for the sodium insertion process in TpPa-SO_3H@CNT-50 and TpPa-SO_3H@Graphene. Ex situ XPS was used to study any variations in the states of the elements within the materials prior to and following sodium insertion taking particular note of changes in O atoms, the main adsorption sites for Na^+. As mentioned previously, the bonding energy of C═O and S—O in TpPa-SO_3H@CNT-50 shows a shift to a lower energy state (C═O: 531.87 eV, S—O: 530.23 eV) compared to those of TpPa-SO_3H@Graphene (C═O: 532.50 eV, S250O: 530.65 eV) (**Figure 5**a), indicating the greater activity of the O sites for sodium ion adsorption in the curved COF grown on CNT. This change is consistent with the CV analysis where the redox peak of TpPa-SO_3H@CNT-50 shifts to zero potential compared to that of TpPa-SO_3H@Graphene, indicating an easier activation of the adsorption sites in TpPa-SO_3H@CNT-50 (Figure S10a, Supporting Information). Following the insertion of sodium ions, C═O and S—O in TpPa-SO_3H@CNT-50 maintain a lower binding energy state than those in TpPa-SO_3H@Graphene. Notably, two new peaks emerge representing S—O—Na and C—O—Na, indicating the sodium insertion process involving these groups in the framework. Due to the different adsorption activity induced by the local strain effect of CNT and graphene, the binding energy of the new S-O-Na and C-O-Na peaks for TpPa-SO_3H@CNT-50 (S-O-Na: 532.79 eV, C—O—Na: 535.22 eV) also present at lower energy than the corresponding groups in TpPa-SO_3H@Graphene (S-O-Na: 533.11 eV, C—O—Na: 535.8 eV) (Figure 5b). This suggests a higher Na^+ charge/discharge activity for S-O-Na and C-O-Na in the former case (TpPa-SO_3H@CNT-50). This has been confirmed by considering the EIS data analysis mentioned previously in this article (Figure S10f, Supporting Information). Variations in the density-of-states at the Fermi level occurring in the pores of TpPa-SO_3H growing on the different carbon templates, and the structural stability, were further investigated by using VASP AIMD simulations. We note that the density-of-state at the Fermi level is predominantly attributed to the p orbitals of carbon (C) and oxygen (O) atoms contained in the frameworks. As shown in Figure 5a,b, O and C play a central role in establishing connections with Na^+ during the sodium insertion process. This highlights the significance of the specific interactions of O and α-C of β-ketoenamine with sodium ions. The overall density-of-states of curved TpPa-SO_3H on CNT is obviously lower than that of flat TpPa-SO_3H layered on graphene. This further confirms that curved COFs offer increased Na^+ adsorption activity over flat COF, highlighting the importance of local strain and curvature effects on CDI performance. The theoretical calculations are thus consistent with the experimental ex situ XPS analysis.

For further discussing the desalination mechanism of the active materials, the mass transport during the Na^+ adsorption process was discussed via the in situ electrochemical quartz crystal microbalance (EQCM) measurement which has been applied to quantify mass changes during the electrochemical energy storage field. The active material to be interrogated was coated onto an Au-coated quartz crystal sensor and used as the working electrode in a three-electrode cell. An increase in electrode mass causes a decrease in the crystal's oscillation frequency according to the Sauerbrey equation.[49] **Figure 6** shows the EQCM response for the third overtone of the TpPa-SO_3H-COF and corresponding hybrid materials-coated Au-sensor immersed in 500 ppm NaCl aqueous solution during chronoamperometry scan. The EQCM response tracks well with the charge process. Compared to pure TpPa-SO_3H-COF and TpPa-SO_3H@Graphene, TpPa-SO_3H@CNT displays the largest shift in both integrated charge (Q) and frequency (f_3), indicating the largest theoretical Na^+ adsorption capacity and actual total mass increase. The EQCM further confirms that the curved COF shows a great advantage for the Na^+ adsorption in terms of dynamics, agreeing with ex situ XPS analysis and theoretical calculations results.

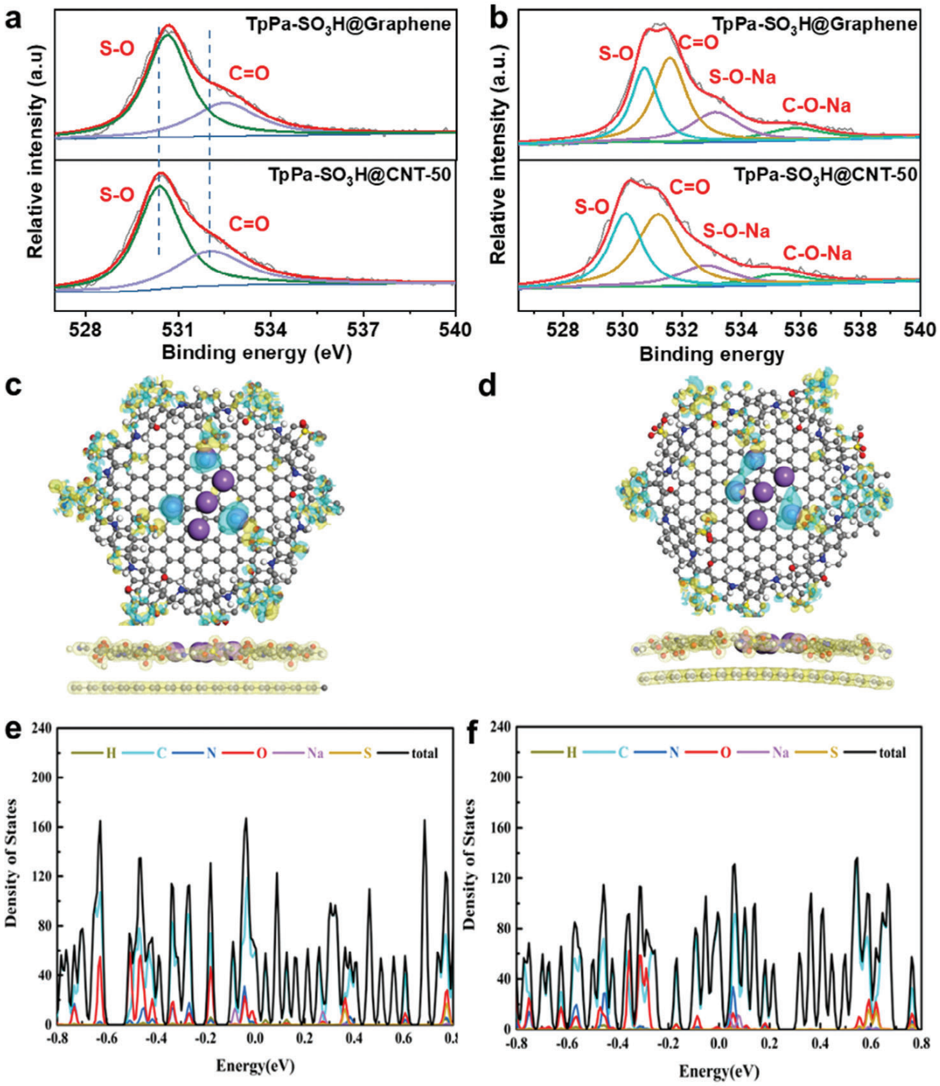

Figure 5. Illustration of the importance of local strain and curve effects on Na$^+$ insertion properties. XPS spectra of the O 1s region of a) TpPa-SO$_3$H@CNT-50 and b) TpPa-SO$_3$H@Graphene before and after sodium ions adsorption. Demonstration of density of state of c,e) TpPa-SO$_3$H@Graphene and d,f) TpPa-SO$_3$H@CNT-50 before and after sodium ions adsorption.

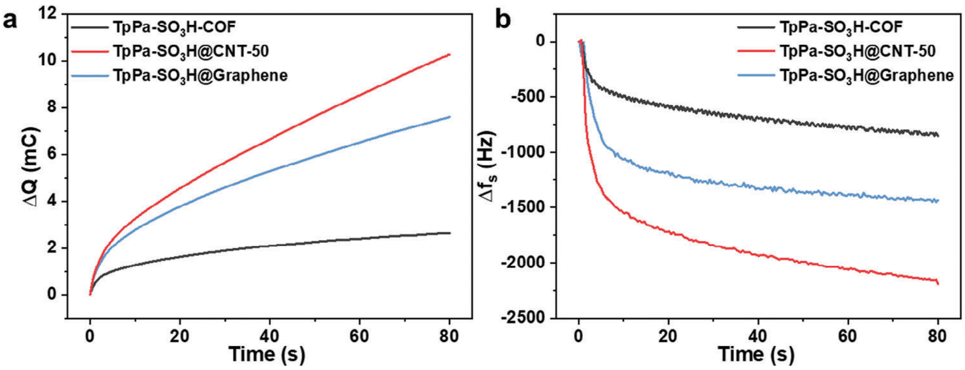

Figure 6. In situ EQCM analysis of TpPa-SO$_3$H-COF, TpPa-SO$_3$H@CNT-50, and TpPa-SO$_3$H@Graphene during chronoamperometry scan at the potential of 1.0 V versus Ag/AgCl in 500 ppm NaCl aqueous solution. a) Integrated charge and b) f_3 responses.

3. Conclusion

In summary, a curved COF layer formed by controlled growth on CNT template has been designed and constructed for deliberate enhancement of the desalination performance and to study the effect of COF curvature on CDI performance. A detailed structure-function relationship underlying the diverse Na$^+$ charge/discharge properties is demonstrated. CNT-induced curved COF shows easier activation for the insertion of sodium ions compared to flat COF grown on graphene. This important feature is confirmed by applying ex situ X-ray photoelectron spectroscopy analysis. The overall density-of-states of curved TpPa-SO$_3$H on CNT is lower than that of flat TpPa-SO$_3$H layered on graphene, further confirming that curved COF has better Na$^+$ adsorption activity than flat COF, in turn highlighting the importance of local strain and curvature effects on CDI performance. Local strain induces lower binding energy states of the adsorption sites in the COF structures, thus facilitating the sodium insertion process. Thus, curved COF materials show remarkable CDI performances with large ion adsorption capacity for Na$^+$ (IAC (Na$^+$)) of 58.74 mg g^{-1} and high Na$^+$ adsorption rate (IAR (Na$^+$)) of 1.96 mg g^{-1} min^{-1} in 1000 ppm NaCl solution at 1.2 V, as well as a very high salt (NaCl) adsorption capacity (SAC (NaCl)) of 149.25 mg g^{-1} for the whole cell. This ultrahigh Na$^+$ adsorption capacity is significantly greater than that of the control flat COF materials that include a COF@Graphene hybrid and pristine COF. This discovery will open new avenues to design enhanced activity COFs or other conventional 2D materials for capacitive deionization applications.

Supporting Information

Supporting Information is available from the Wiley Online Library or from the author.

Acknowledgements

D.J. and R.X. contributed equally to this work. The authors acknowledge financial support from the JST-ERATO Yamauchi Materials Space-Tectonics Project (JPMJER2003), the ARC Australian Laureate Fellowship (FL230100095), and the UQ-Yonsei International Joint Research Project. This work used the Queensland node of the NCRIS-enabled Australian National Fabrication Facility (ANFF). Y.K. thanks the support from JSPS Postdoctoral Fellowships for Research in Japan. The authors demonstrate the appreciation for English editing software such as ChatGPT, Grammarly, etc.

Open access publishing facilitated by The University of Queensland, as part of the Wiley - The University of Queensland agreement via the Council of Australian University Librarians.

Conflict of Interest

The authors declare no conflict of interest.

Data Availability Statement

The data that support the findings of this study are available in the supplementary material of this article.

Keywords

capacitive deionization, covalent organic frameworks (COFs), curvature engineering, regulation of charge distribution

Received: May 1, 2024
Revised: August 1, 2024

---

[1] P. Srimuk, X. Su, J. Yoon, D. Aurbach, V. Presser, *Nat. Rev. Mater.* **2020**, *5*, 517.
[2] F. He, P. M. Biesheuvel, M. Z. Bazant, T. A. Hatton, *Water Res.* **2018**, *132*, 282.
[3] X. Xu, J. Tang, Y. V. Kaneti, H. Tan, T. Chen, L. Pan, T. Yang, Y. Bando, Y. Yamauchi, *Mater. Horiz.* **2020**, *7*, 1412.
[4] M. E. Suss, S. Porada, X. Sun, P. M. Biesheuvel, J. Yoon, V. Presser, *Energy Environ. Sci.* **2015**, *8*, 2296.
[5] Z. Wang, X. Xu, J. Kim, V. Malgras, R. Mo, C. Li, Y. Lin, H. Tan, J. Tang, L. Pan, Y. Bando, T. Yang, Y. Yamauchi, *Mater. Horiz.* **2019**, *6*, 1437.
[6] X. Liu, X. Xu, X. Xuan, W. Xia, G. Feng, S. Zhang, Z. Wu, B. Zhong, X. Guo, K. Xie, Y. Yamauchi, *J. Am. Chem. Soc.* **2023**, *145*, 9242.
[7] X. Gao, A. Omosebi, J. Landon, K. Liu, *Environ. Sci. Technol.* **2015**, *49*, 10920.
[8] J. S. Kang, S. Kim, D. Y. Chung, Y. J. Son, K. Jo, X. Su, M. Lee, H. J. Jae, T. A. Hatton, J. Yoon, Y.-E. Sung, *Adv. Funct. Mater.* **2020**, *30*, 1909387.
[9] J. G. Gamaethiralalage, K. Singh, S. Sahin, J. Yoon, M. Elimelech, M. E. Suss, P. Liang, P. M. Biesheuvel, R. L. Zornitta, L. C. P. M. de Smet, *Energy Environ. Sci.* **2021**, *14*, 1095.
[10] K. Kim, S. Cotty, J. Elbert, R. Chen, C.-H. Hou, X. Su, *Adv. Mater.* **2020**, *32*, 1906877.
[11] K. Sun, M. Tebyetekerwa, C. Wang, X. Wang, X. Zhang, S. X. Zhao, *Adv. Funct. Mater.* **2023**, *33*, 2213578.
[12] Z.-H. Huang, Z. Yang, F. Kang, M. Inagaki, *J. Mater. Chem.* **2017**, *5*, 470.
[13] Q. Li, Y. Zheng, D. Xiao, T. Or, R. Gao, Z. Li, M. Feng, L. Shui, G. Zhou, X. Wang, Z. Chen, *Adv. Sci.* **2020**, *7*, 2002213.
[14] H. Wang, B. Chen, D.-J. Liu, X. Xu, L. Osmieri, Y. Yamauchi, *Small* **2022**, *18*, 2102477.
[15] Z. Wang, C. Wang, Y. Chen, L. Wei, *Adv. Mater. Technol.* **2023**, *8*, 2201828.
[16] P. Simon, Y. Gogotsi, *Nat. Mater.* **2020**, *19*, 1151.
[17] C. Zhang, D. He, J. Ma, W. Tang, T. D. Waite, *Water Res.* **2018**, *128*, 314.
[18] R. Liu, K. T. Tan, Y. Gong, Y. Chen, Z. Li, S. Xie, T. He, Z. Lu, H. Yang, D. Jiang, *Chem. Soc. Rev.* **2021**, *50*, 120.
[19] S. Kandambeth, K. Dey, R. Banerjee, *J. Am. Chem. Soc.* **2019**, *141*, 1807.
[20] C. S. Diercks, O. M. Yaghi, *Science* **2017**, *355*, eaal1585.
[21] L. Zhou, S. Jo, M. Park, L. Fang, K. Zhang, Y. Fan, Z. Hao, Y.-M. Kang, *Adv. Energy Mater.* **2021**, *11*, 2003054.
[22] S. Kandambeth, V. S. Kale, O. Shekhah, H. N. Alshareef, M. Eddaoudi, *Adv. Energy Mater.* **2022**, *12*, 2100177.
[23] X. Li, S. Cai, B. Sun, C. Yang, J. Zhang, Y. Liu, *Matter* **2020**, *3*, 1507.
[24] A. Jrad, M. A. Olson, A. Trabolsi, *Chem* **2023**, *9*, 1413.
[25] D. Liu, X. Ning, Y. Hong, Y. Li, Q. Bian, J. Zhang, *Electrochim. Acta.* **2019**, *296*, 327.
[26] Y. Li, Z. Ding, X. Zhang, J. Li, X. Liu, T. Lu, Y. Yao, L. Pan, *J. Mater. Chem. A* **2019**, *7*, 25305.
[27] H. Gao, Q. Zhu, A. R. Neale, M. Bahri, X. Wang, H. Yang, L. Liu, R. Clowes, N. D. Browning, R. S. Sprick, M. A. Little, L. J. Hardwick, A. I. Cooper, *Adv. Energy Mater.* **2021**, *11*, 2101880.

[28] O. J. Wahab, E. Daviddi, B. Xin, P. Z. Sun, E. Griffin, A. W. Colburn, D. Barry, M. Yagmurcukardes, F. M. Peeters, A. K. Geim, M. Lozada-Hidalgo, P. R. Unwin, *Nature.* **2023**, *620*, 782.

[29] F. Xu, S. Jin, H. Zhong, D. Wu, X. Yang, X. Chen, H. Wei, R. Fu, D. Jiang, *Sci. Rep.* **2015**, *5*, 8225.

[30] S. Kumar, N. M. Aldaqqa, E. Alhseinat, D. Shetty, *Angew. Chem.Int. Ed.* **2023**, *62*, 202302180.

[31] J. Sun, A. Klechikov, C. Moise, M. Prodana, M. Enachescu, A. V. Talyzin, *Angew. Chem., Int. Ed.* **2018**, *57*, 1034.

[32] V. Eckert, E. Haubold, S. Oswald, S. Michel, C. Bellmann, P. Potapov, D. Wolf, S. Hampel, B. Büchner, M. Mertig, A. Leonhardt, *Carbon N. Y.* **2019**, *141*, 99.

[33] N. Ma, Y. Zhang, Y. Wang, J. Zhao, B. Liang, Y. Xiong, S. Luo, C. Huang, J. Fan, *J. Colloid. Interface Sci.* **2024**, *654*, 1458.

[34] G.-L. Chai, Z. Hou, D.-J. Shu, T. Ikeda, K. Terakura, *J. Am. Chem. Soc.* **2014**, *136*, 13629.

[35] J. Moreno, S. Aspera, M. David, H. Kasai, *Carbon* **2015**, *94*, 936.

[36] D. Jiang, X. Xu, Y. Bando, S. M. Alshehri, M. Eguchi, T. Asahi, Y. Yamauchi, *B. Chem. Soc. Jpn.* **2024**, uoae074.

[37] S. Kandambeth, A. Mallick, B. Lukose, M. V. Mane, T. Heine, R. Banerjee, *J. Am. Chem. Soc.* **2012**, *134*, 19524.

[38] Y. Xu, P. Cai, K. Chen, Q. Chen, Z. Wen, L. Chen, *Angew. Chem., Int. Ed.* **2023**, *62*, 20221558.

[39] S. Chandra, T. Kundu, K. Dey, M. Addicoat, T. Heine, R. Banerjee, *Chem. Mater.* **2016**, *28*, 1489.

[40] M. C. Daugherty, E. Vitaku, R. L. Li, A. M. Evans, A. D. Chavez, W. R. Dichtel, *Chem. Commun.* **2019**, *55*, 2680.

[41] C. R. DeBlase, K. E. Silberstein, T.-T. Truong, H. D. Abruña, W. R. Dichtel, *J. Am. Chem. Soc.* **2013**, *135*, 16821.

[42] K. Jeong, S. Park, G. Y. Jung, S. H. Kim, Y.-H. Lee, S. K. Kwak, S.-Y. Lee, *J. Am. Chem. Soc.* **2019**, *141*, 5880.

[43] Y. Peng, G. Xu, Z. Hu, Y. Cheng, C. Chi, D. Yuan, H. Cheng, D. Zhao, *ACS Appl. Mater. Interfaces* **2016**, *8*, 18505.

[44] P. Hu, H. Wang, Y. Yang, J. Yang, J. Lin, L. Guo, *Adv. Mater.* **2016**, *28*, 3486.

[45] Z. Lei, Q. Yang, Y. Xu, S. Guo, W. Sun, H. Liu, L.-P. Lv, Y. Zhang, Y. Wang, *Nat. Commun.* **2018**, *9*, 576.

[46] S. Gu, S. Wu, L. Cao, M. Li, N. Qin, J. Zhu, Z. Wang, Y. Li, Z. Li, J. Chen, Z. Lu, *J. Am. Chem. Soc.* **2019**, *141*, 9623.

[47] G. Zhao, L. Xu, J. Jiang, Z. Mei, Q. An, P. Lv, X. Yang, H. Guo, X. Sun, *Nano Energy* **2022**, *92*, 106756.

[48] M. R. Lukatskaya, O. Mashtalir, C. E. Ren, Y. D. Agnese, P. Rozier, P. L. Taberna, M. Naguib, P. Simon, M. W. Barsoum, Y. Gogotsi, *Science* **2013**, *341*, 1502.

[49] S. Wang, F. Li, A. D. Easley, J. L. Lutkenhaus, *Nat. Mater.* **2019**, *18*, 69.